Space Weather

RESEARCH ARTICLE
10.1029/2019SW002168

Special Section:
Space Weather Events of 4-10 September 2017

Response of the Ionosphere-Plasmasphere Coupling to the September 2017 Storm: What Erodes the Plasmasphere so Severely?

Yuki Obana[1], Naomi Maruyama[2,3], Atsuki Shinbori[4], Kumiko K. Hashimoto[5], Mariangel Fedrizzi[2,3], Masahito Nosé[4], Yuichi Otsuka[4], Nozomu Nishitani[4], Tomoaki Hori[4], Atsushi Kumamoto[6], Fuminori Tsuchiya[7], Shoya Matsuda[8], Ayako Matsuoka[8], Yoshiya Kasahara[9], Akimasa Yoshikawa[10], Yoshizumi Miyoshi[4], and Iku Shinohara[8]

[1]Department of Engineering Science, Faculty of Engineering, Osaka Electro-Communication University, Neyagawa, Japan, [2]CIRES, University of Colorado Boulder, Boulder, CO, USA, [3]NOAA Space Weather Prediction Center, Boulder, CO, USA, [4]Institute for Space-Earth Environmental Research (ISEE), Nagoya University, Nagoya, Japan, [5]School of Agriculture, Kibi International University, Minamiawaji, Japan, [6]Department of Geophysics, Tohoku University, Sendai, Japan, [7]Planetary Plasma and Atmospheric Research Center (PPARC), Tohoku University, Sendai, Japan, [8]Institute of Space and Astronautical Science, Japan Aerospace Exploration Agency, Sagamihara, Japan, [9]Graduate School of Natural Science and Technology, Kanazawa University, Kanazawa, Japan, [10]Department of Earth and Planetary Sciences, Kyushu University, Fukuoka, Japan

Key Points:
- An extreme erosion of the plasmasphere was observed by the ERG/Arase spacecraft (L_P1.6–1.7)
- The trough minimum location identified in GNSS-TEC moved equatorward as low as ~48 degree magnetic latitude (L = ~2.2)
- The observed erosion was qualitatively reproduced by the IPE simulation by including the effect of the penetration electric field

Correspondence to:
Y. Obana,
obana@osakac.ac.jp

Citation:
Obana, Y., Maruyama, N., Shinbori, A., Hashimoto, K. K., Fedrizzi, M., Nosé, M., et al. (2019). Response of the ionosphere-plasmasphere coupling to the September 2017 storm: What erodes the plasmasphere so severely? *Space Weather*, *17*, 861–876. https://doi.org/10.1029/2019SW002168

Received 29 JAN 2019
Accepted 3 MAY 2019
Accepted article online 18 MAY 2019
Published online 19 JUN 2019

Abstract We report an extreme erosion of the plasmasphere arising from the September 2017 storm. The cold electron density is identified from the upper limit frequency of upper hybrid resonance waves observed by the Plasma Wave Experiment instrument onboard the Exploration of energization and Radiation in Geospace/Arase satellite. The electron density profiles reveal that the plasmasphere was severely eroded during the recovery phase of the storm and the plasmapause was located at L = 1.6–1.7 at 23 UT 8 September 2017. This is the first report of deep erosion of the plasmasphere ($L_{PP} < 2$) with the in situ observation of the electron density. The degree of the severity is much more than what is expected from the relatively moderate value of the SYM-H minimum (−146 nT). We attempt to find a possible explanation for the observed severe depletion by using both observational evidence and numerical simulations. Our results suggest that the middle latitude electric field had penetrated from the high-latitude storm time convection for several hours. Such an unusually long-lasting penetration event can cause this observed degree of severity.

Plain Language Summary The plasmasphere is the region of cold, relatively dense ionized gas (mostly protons and helium ions) that resides on the magnetic field lines close to the Earth. It is understood that the plasmasphere is threaded by magnetic field flux tubes that are persistently "closed," so that plasma from the Earth's ionosphere has filled the flux tubes. The typical location of the outer boundary of the plasmasphere, known as the plasmapause, is usually 40,000–50,000 km from the Earth. Here we report that a magnetic storm during 7–10 September 2017 dramatically displaced the outer boundary of the plasmasphere inwards, to only ~4,000 km from Earth's surface. Our study suggests that the remarkable deformation is caused by the unusually long-lasting leakage of the convection electric field deep within the plasmasphere.

1. Introduction

The plasmasphere is the corotating reservoir region of cold, relatively dense ionized gas (mostly electrons, protons, and helium ions) that resides on the magnetic field lines close to the Earth (e.g., Carpenter & Park, 1973). During geomagnetically quiet periods, the plasmasphere is thought to expand as flux tubes slowly fill with cold plasma from the ionosphere. During geomagnetically active times when solar wind-magnetosphere coupling becomes strong, magnetospheric convection strips off the outer layers of the plasmasphere, and the plasmaspheric materials are transported from the near-Earth reservoir to the sunward boundary of the magnetosphere, so-called erosion (e.g., Goldstein, 2006; Nishida, 1966). The outer plasmasphere is depleted, forming a plasmatrough. As a consequence, the outer boundary of the plasmasphere, known as the plasmapause, is brought closer to the Earth (e.g., Chappell et al., 1970). The plasmapause

motion is very dynamic, and its spatial structure and location are highly dependent on the relative balance between the corotation electric field and the sunward convection due to the solar wind-magnetosphere interaction. The smallest plasmapause radius ever reported in the recent literature is 1.5 Earth radii (L_P1.5 R_E) during the famous Halloween storm (Baker et al., 2004). In this study, plasmapause locations were inferred from the extreme ultraviolet (EUV) images obtained by the Imager for Magnetopause-to-Aurora Global Exploration (IMAGE) spacecraft. The highest value of the cross polar cap potential drop was found to be 225 kV based on the observations from the Defense Meteorological Satellite Program-F13 spacecraft during the Halloween storm (Hairston et al., 2005).

Prediction of the evolution of the plasmasphere and plasmapause location is very critical in understanding dynamics of plasma populations in the inner magnetosphere because the plasmasphere, ring current, and radiation belts form a closely coupled system in this region. For example, plasmasphere composition controls the excitation of electromagnetic ion cyclotron waves, which in turn scatter the ring current and radiation belt particles into the loss cone (e.g., Summers & Thorne, 2003). The locations of the plasmapause and plumes define the region of radiation belt particles interacting with whistler mode chorus or hiss waves (e.g., Li et al., 2006; Shprits et al., 2006). In addition, because of the inertia, the dense and cold plasmaspheric plasma may affect the dayside magnetic reconnection (e.g., Borovsky, 2014; Walsh et al., 2014).

To predict the plasmapause location, many previous authors have developed empirical models as a function of ground-based geomagnetic indices (e.g., Carpenter & Anderson, 1992; Goldstein et al., 2014; Moldwin et al., 2002; O'Brien & Moldwin, 2003). However, when it comes to accurately predicting the plasmaspheric dynamics, the plasmapause location, or for individual events, it still remains very challenging since the drivers of the plasmaspheric cold plasmas are dynamically changing and the underlying mechanisms cannot be completely elucidated, in particular, as the temporal evolution of the solar wind-magnetospheric interaction and magnetospheric flow becomes more complicated.

In this paper, we report on an unusually severe depletion of the plasmasphere electron density during the 7–10 September 2017 storm period observed by the Plasma Wave Experiment (PWE) instrument (Kasahara et al., 2018) onboard the Arase (ERG, Exploration of energization and Radiation in Geospace) spacecraft (Miyoshi, Shinohara, et al., 2018). The main purpose of this study is to investigate the severity of the depletion in the plasmasphere during the storm event and to suggest a possible mechanism that generates the depletion. We address the science question by combining multiple observations data and physics-based model simulations from both the ionosphere and plasmasphere viewpoints. The outline of this paper is as follows: Section 2 describes the event studied. Section 3 describes the data and the physics-based model of the ionosphere, plasmasphere, and electrodynamics (IPE) used in this study. Section 4 describes the results from the observations and model simulations. Discussions and conclusions are, respectively, made in sections 5 and 6.

2. Event Description

The event studied covers the period of 4–10 September 2017 (SYM-H $_{\min}$ −146 nT, $K_{p\ \max}$ 8^{+}) during which the most intense solar flare within solar cycle 24 and three coronal mass ejections were launched. The associated interplanetary shocks led to extreme solar wind conditions. The considerable periods of the large southward B_z excursion resulted in the dayside magnetopause being pushed inside geosynchronous orbit as observed by the GOES 13 and 15 spacecraft at ~1400 UT on 8 September (Redmon et al., 2018). Figure 1 shows the temporal variation of (a) the solar wind velocity, (b) the Geocentric Solar Magnetospheric components of the interplanetary magnetic field (IMF) measured at L1 (~1.42 × 10^6 km from Earth, time shifted to the subsolar magnetopause location) by the Wind and ACE satellites, (c) the cross polar cap potential drop values and the dawn-to-dusk component of the interplanetary electric field (IEF_y), (d) the SYM-H index, and (e) the K_p index during the interval from 0000 UT on 7 September to 2400 UT on 8 September. The solar wind data are provided by the OMNI website and time shifted to the Earth's bow shock nose. The cross polar cap potential drop is initially calculated from 5-min averages of solar wind and IMF data using the empirical relations of Boyle et al. (1997) but modified to include the cross polar cap potential saturation effect (e.g., Hairston et al., 2003). The geomagnetic storm commenced at 2300 UT on 7 September as a sudden increase of the SYM-H index. The IMF B_z turned southward down to −32 nT when the solar wind velocity suddenly increased by ~230 km/s. The subsequent increase in the cross polar cap potential

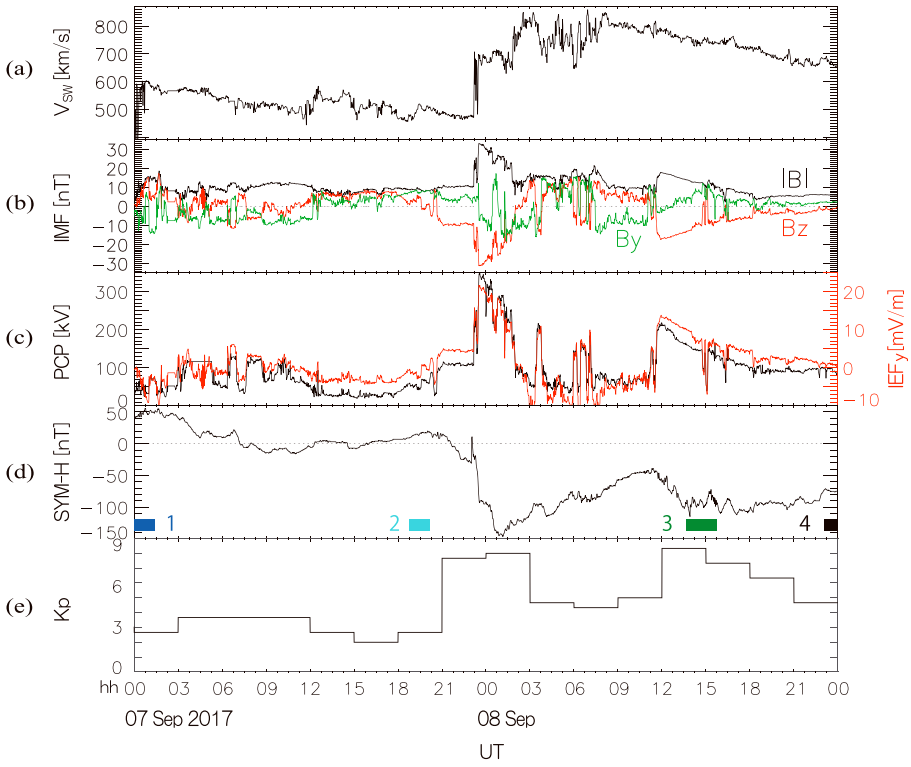

Figure 1. (a) Solar wind velocity; (b) total interplanetary magnetic field (IMF) field|*B*|measured by the Wind and ACE spacecraft (black curve), IMF geocentric solar magnetospheric components measured at L1 (~1.42×10^6 km from Earth, time shifted to the subsolar magnetopause location) by the Wind and ACE satellites, IMF B_z component (red curve), and IMF B_y component (green curve); (c) estimated cross polar cap potential drop (black curve) and the dawn-to-dusk component of the interplanetary electric field (IEF_y; red curve); (d) SYM-H index; (e) K_p index, during 7–8 September 2017. The blue, cyan, green, and black bars shown in panel (d) indicate the time corresponding to the orbits shown in Figure 3.

drop reached the peak value of 235 kV at ~0025 UT on 8 September. SYM-H $_{min}$ ($K_{p\ max}$) reached −146 nT (8) at ~0110 UT (during 0–3 UT), followed by a recovery until the second major southward turning of IMF B_z, which occurred at ~1130 UT on 8 September, resulting in an increase in the cross polar cap potential drop in excess of 246 kV. SYM-H $_{min}$ ($K_{p\ max}$) reached −115 nT (8^+) at ~0110 UT (during 12–15 UT). It is interesting to note that $K_{p\ max}$ in the second main phase was larger than that in the first main phase. The cross polar cap potential drop gradually decreases to 100 kV by the end of 8 September. The corresponding recovery of SYM-H is also very slow. The dawn-to-dusk component of the interplanetary electric field, as shown by the red line in Figure 1c, is calculated by using the solar wind velocity and the IMF B_z ($IEF_y = -V_{SW} \times B_z$). It is considered as the source of the penetrating electric field throughout the magnetosphere-ionosphere system from the dayside reconnection line during geomagnetically active periods (e.g., Kelley et al., 2003).

3. Observations and Modeling

3.1. Electron Density Obtained From Arase/PWE Data

We estimate the electron number density along the Arase orbit using the upper hybrid resonance (UHR) emissions. The UHR waves are often observed in the inner magnetosphere with a narrow-banded spectrum. From the upper-limit frequency of the UHR waves (f_{UHR}), the electron density along the spacecraft orbit is easily estimated.

$$f_{UHR}{}^2 = f_{ce}{}^2 + f_{pe}{}^2,$$

where f_{ce} and f_{pe} are the local electron cyclotron frequency and electron plasma frequency, respectively.

Substituting appropriate values for the electron charge and mass, the electron number density n_e is calculated by

$$n_e = \frac{{f_{\mathrm{UHR}}}^2 - {f_{ce}}^2}{8,980},$$

where density and frequencies are expressed in cubic centimeters and in hertz, respectively.

The ERG/Arase project is a Japanese mission to investigate acceleration and loss mechanisms of relativistic electrons around the Earth (Miyoshi, Shinohara, et al., 2018). The spacecraft was launched on 20 December 2016 from Uchinoura Space Center and has been put into a geo-transfer orbit with an inclination of 31°, with initial apogee, perigee, and the orbital period of 32,110 km, 460 km, and 565 min, respectively (Miyoshi, Shinohara, et al., 2018). The High Frequency Analyzer (HFA) is a subsystem of the Plasma Wave Experiment (PWE) onboard the Arase spacecraft for the observation of radio and plasma waves. The HFA provides the spectrograms of electric fields in a frequency range from 10 kHz to 10 MHz with an 8-s time resolution (Kasahara et al., 2018; Kumamoto et al., 2018). In this study, HFA spectrograms are visually inspected to identify f_{UHR}. Electron density is obtained by converting from the f_{UHR} with 8-s spin average total magnetic field intensity measured by the Magnetic Field Experiment instrument (Matsuoka et al., 2018) also onboard the Arase satellite. The Common Data Format data of the HFA plasma wave spectrum are provided by ERG Science Center, Nagoya University, Japan (Miyoshi, Hori, et al., 2018).

3.2. Absolute GNSS-TEC (ATEC) Data

To identify the location of the midlatitude ionospheric trough (which generally serves as a good indicator of plasmapause location; e.g., Anderson et al., 2008; Yizengaw & Moldwin, 2005), the temporal and spatial variations of the absolute Global Navigation Satellite Systems (GNSS)-Total Electron Content (TEC) are investigated. We use the Absolute GNSS-TEC (ATEC) data with time resolution of 30 s obtained from many dense regional and worldwide international GNSS receiver networks.

Detailed information of this GNSS-TEC database and its derivation method are described by Tsugawa et al. (2007, 2018). A detailed method to derive the absolute vertical GNSS-TEC data is found in Otsuka et al. (2002). In this study, we perform a 5-min average of the available grid GNSS-TEC data having a spatial resolution of $0.5 \times 0.5°$ in geographical latitude and longitude. The grid data are running averaged with the data included in four bins. We further calculate the ratio of the difference between storm time ATEC and average ATEC of 10 geomagnetically quiet days every month to the average quiet day ATEC, hereafter called ratio of difference ATEC. Detailed description of the absolute GNSS-TEC analysis and identification of the location of the midlatitude trough minimum is in Shinbori et al. (2018).

3.3. Ground-Based Magnetic Field Observations

To study the penetration of the convection electric field to the equator, we compare magnetic data at low latitude and the dip equator. Assuming that magnetic field variations at the dip equator and low latitude are similarly affected by magnetospheric currents, the difference between the variations at the dip equator and those at low latitude yield the fluctuations caused by ionospheric currents driven by the convection/overshielding electric fields (e.g., Hashimoto et al., 2017).

The four ground-based magnetometer observatories used in this study are listed in Table 1. Three stations (Huancayo: HUA, $L = 1.00$; San Juan: SJG, 1.24; and Kanoya: KNY, 1.21) are part of INTERMAGNET operated by Instituto Geofisico del Perú, U.S. Geological Survey (USGS), and Japan Meteorological Agency, respectively. The other station (Davao: DAV, $L = 1.00$) belongs to the Magnetic Data Acquisition System (MAGDAS) array (Yumoto and the MAGDAS group, 2006) operated by the International Centre for Space Weather Science and Education, Kyushu University, Japan. In converting geographic coordinates to geomagnetic coordinates, we use the Altitude Adjusted Corrected GeoMagnetic model (Baker & Wing, 1989). L values of each station are calculated tracing International Geomagnetic Reference Field (IGRF) 15 field lines to the apex of the field line using the Apex Model (Richmond, 1995). The difference of the north-south component (ΔX) of the geomagnetic field between HUA and SJG and between DAV and KNY is used to infer the storm time response of the equatorial electrojet (EEJ) and the zonal electric field (e.g., Anderson et al., 2002) in the American and the East Asian meridians, respectively.

Table 1
Location of Ground-Based Magnetometer Stations

Code	Station name	Geographic latitude, degrees	Geographic longitude, degrees	AACGM latitude, degrees	AACGM longitude, degrees	*L* value	LT (UT+), hr
HUA	Huancayo	−12.05	284.67	1.45	356.11	1.00	−5.02
SJG	San Juan	18.11	293.85	28.79	9.83	1.24	−4.41
DAV	Davao	7.00	125.40	−1.02	196.54	1.00	8.36
KNY	Kanoya	31.42	130.88	24.44	202.54	1.21	8.73

Note. AACGM = Altitude Adjusted Corrected GeoMagnetic; HUA = Huancayo; SJG = San Juan; DAV = Davao; KNY = Kanoya.

3.4. The SuperDARN Hokkaido Radars

The SuperDARN (Super Dual Auroral Radar Network) are globally networked HF radars measuring backscatter from the ionosphere (Greenwald et al., 1995). The fields of view of more than half of the SuperDARN radars cover the high-latitude regions, whereas the SuperDARN Hokkaido East and Hokkaido West radars (both east and west facing radars are at 43.5°N, 143.6°E), as well as other midlatitude SuperDARN radars, have their fields of view covering the subauroral regions (Nagano et al., 2015). The measurements of Doppler velocity obtained from the Hokkaido radars are used to study the penetration of the electric field to middle latitudes.

3.5. The IPE Model

The IPE model (Maruyama et al., 2016; Sun et al., 2015) is used to understand the dynamics of the plasmasphere that results in the unusually severe depletion observed by the Arase measurements. The IPE model is based on the well-tested, one-dimensional, Field Line Interhemispheric Plasma model (Richards et al., 2010).

In order to make three-dimensional, global coverage, the IPE simulations in this study use a total of 7,440 flux tubes with 93 in latitude and 80 in longitude directions. In this study, the longitudinal resolution is 4.5°, while the latitudinal resolution is variable with an average latitudinal resolution of approximately 0.34°. The spatial resolution of the radial direction varies from 0.05 R_E ($L = 1.5$) to 0.46 R_E ($L = 5$). The latitude of the most poleward flux tube is 88.2°. No altitude boundary is necessary because all the flux tubes are closed, which provides an advantage of coupling ionosphere and plasmasphere self-consistently. The arc length between two grid points along the magnetic grid has been designed to be less than the plasma scale height in the *F* region. The number of grid points along a field line ranges from 11 near the equator to 1,115 at the highest latitude. IPE uses the Apex coordinates (Richmond, 1995) based on the IGRF-10 (Maus et al., 2005). The realistic representation of the Earth's magnetic field enables more accurate studies of the longitudinal and UT dependencies globally. Furthermore, global perpendicular **E×B** transport has been included as well, which is updated every 5 s, while the parallel transport (the calling frequency of Field Line Interhemispheric Plasma) is every 60 s.

Photoionization rates and photoelectron fluxes are calculated using the combination of the solar EUV irradiance model for aeronomic calculations EUVAC (Richards et al., 1994) and HEUVAC (Richards et al., 2006). HEUVAC is a high-resolution version of EUVAC, including the irradiances below 50 Å that are important for photoelectron production. Both models are driven by the average between the daily $F_{10.7}$ and the 81-day running mean values of the daily $F_{10.7}$, both of which are set to 129 on 8 September 2017 in the IPE simulations in this study.

The thermospheric temperatures and number densities are obtained from the NRL Mass Spectrometer, Incoherent Scatter Radar Extended (NRLMSISE-00) model (Picone et al., 2002). The winds are from the Horizontal Wind Model (Hedin et al., 1996), although the model now has an option to couple to the Whole Atmosphere Model (Akmaev et al., 2008; Fuller-Rowell et al., 2008). The coupled model has been running 24/7 on the NOAA Super Computers in a test operational mode since October 2017 (Maruyama et al., 2017). The geomagnetic activity index is set to the constant value $A_p = 4$ for MSIS/HWM.

The storm time response of the plasmaspheric electron density is realized by the time-dependent, high-latitude drivers of the cross polar cap potential drop (Weimer, 1996) and auroral precipitation (Fuller-

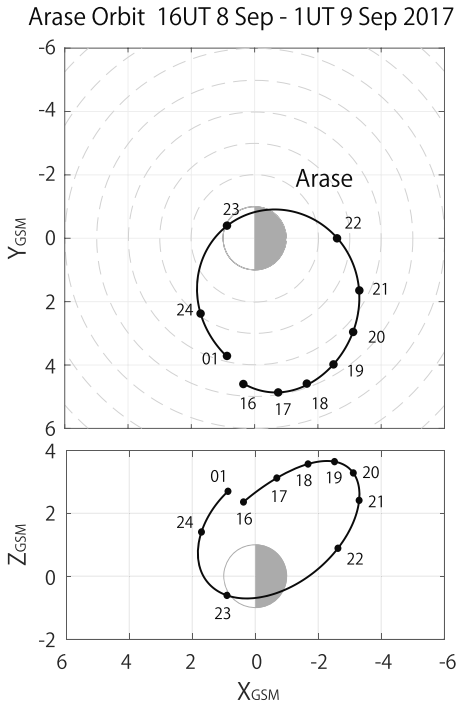

Figure 2. The Exploration of energization and Radiation in Geospace/Arase orbit at 1700 UT 8 September to 0200 UT 9 September 2017 in the *X-Y* plane (top) and the *X-Z* plane (bottom) in the geocentric solar magnetospheric (GSM) coordinates. The orbit has its apogee in the duskside. The inbound and outbound are, respectively, in the nightside and the dayside.

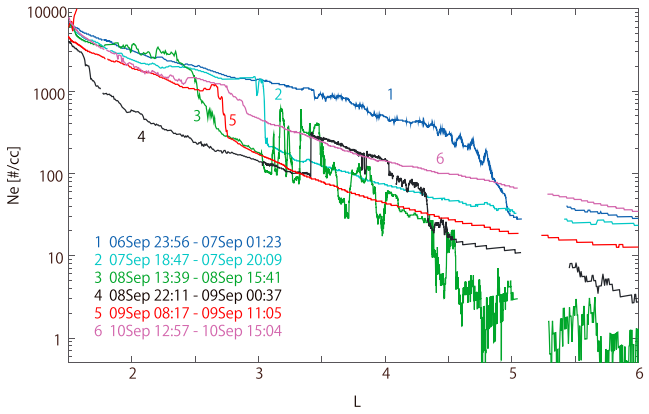

Figure 3. Arase observations of cold electron density profiles as a function of McIlwain's *L* parameter. The exact times of each observation are shown in the figure. All observations are from outbound orbits. Blue: quiet time plasmasphere before the storm, being spread to $L = 4.8–5.0$. Cyan: initial erosion of the outer plasmasphere at $L = 3.0–5.0$ and the plasmapause steepening at $L = 3.0$ as the storm progresses. Green: the plasmapause pushed further equatorward at $L = 2.5$ during the first cross polar cap potential drop enhancement. Black: the most severely eroded plasmasphere with the plasmapause being pushed even further at $L = 1.6–1.7$ immediately after the second recovery phase. Red: partial recovery of the severely eroded plasmasphere at 9 hr after the density profile #4 (black).

Rowell & Evans, 1987). In this study, the global coverage of the electric fields is provided by including the midlatitude and low-latitude empirical model of Scherliess and Fejer (1999), although the model now has an option to self-consistently calculate the midlatitude and low-latitude electric potential based on the global ionospheric electrodynamic solver (Richmond & Maute, 2014). The auroral particle ionization rate profiles are evaluated based on the statistical maps of auroral energy influx and characteristic energy, developed by measurements from the TIROS-NOAA polar orbiting satellites (Fuller-Rowell & Evans, 1987). The maps of the potential, auroral energy flux, and characteristic energy are updated every minute by using the solar wind parameters as shown in Figure 1.

IPE has been applied to understanding the ionospheric response to sudden stratospheric warming (Millholland et al., 2013), the Southern Hemisphere Midlatitude Summer Nighttime Anomaly/Weddell Sea anomaly (Sun et al., 2015), and the three peak structure (Maruyama et al., 2016). Further detailed description of the IPE model is in Maruyama et al. (2016) and Sun et al. (2015).

4. Results

4.1. Deep Erosion of the Plasmasphere

Figure 2 shows the orbital segment of the Arase spacecraft during the interval from 1600 UT on 8 September to 0100 UT on 9 September 2017 in the *X-Y* plane (top) and *X-Z* plane (bottom). During our analysis period, Arase had a perigee in the dawnside and an apogee in the duskside and flew in the dayside of the magnetosphere in the outbound passes of its orbit. Figure 3 displays the cold electron density profiles as a function of the McIlwain L-parameter (IGRF15 model) (McIlwain, 1961) from the f_{UHR} obtained from Arase/PWE. All of the observations shown in Figure 3 are from Arase's outbound data, so they are electron density in the dayside magnetosphere. The blue line shows the electron density profile in the quiet time before the magnetic storm. The plasmasphere is extensively spread up to $L = 4.8–5.0$. Arase crossed the plasmapause around 16.3 magnetic local time (MLT). In the next profile, shown by the cyan line, electron density at $L = 3.0–5.0$ drops down. The outer plasmasphere has been eroded, and the plasmapause appears as a steep gradient of electron density at $L = 3.0$ and 15.1 MLT. It is probably due to the disturbance starting from 0300 UT on 7 September. The green line shows the electron density profile during the second main phase, which commences at 1200 UT on 8 September. The plasmasphere has been further eroded, and the plasmapause is seen at $L = 2.5$ and 14.7 MLT. The observation time of orbit 4, indicated by the black line, is immediately after the second recovery phase starts. Surprisingly, almost the whole plasmasphere has been eroded and only a slightly dense area remains in the narrow region of $L \leq 1.7$. The decrease in density, which seems to correspond to the plasmapause, begins at $L = 1.6$ and ends at 1.7 around 13.2 MLT. The smooth shape of this black curve between $L = 1.7$ and 3.4 looks like the density profile of the saturated plasmasphere. However, we will note that the density level is very low. For example, Carpenter and Anderson (1992) used the sweep frequency receiver radio measurements onboard ISEE 1 satellite and established a well-known empirical model of electron density, which covers the range of $L = 2.25–8$. Using this model, electron density at $L = 2.25$ is estimated to be 1,590 and 530 [#/cm^3]

for the plasmasphere and the plasmatrough, respectively. Whereas, profile #4 in Figure 3 gives 350 [#/cm^3] at $L = 2.25$. It is also noteworthy that in the black line, there is an increase in the density in $L = 3.4$–4.3. Probably, this is plume, wrapping around the Earth at higher L values (Sandel et al., 2001). The red line shows the electron density profile at 9 hr after the one shown by the black line (profile #4). The electron density at $L \leq 2.7$ has recovered to about half of the prestorm level. Arase flew over the plasmapause at $L = 2.7$ and 15.2 MLT. In the final profile (~38 hr after the profile #4), shown by the magenta line, the entire plasmasphere ($L < 6$ and beyond) has been partially refilled.

The degree of the severity of the plasmaspheric depletion appears to be much larger than what would be expected from the relatively nominal value of the SYM-H $_{\text{min}}$ (−146 nT). The degree of severity almost reached the level of the famous Halloween storm ($D_{st\ \text{min}} = -383$ nT): The observed plasmapause radius was located inside 2 R_E and further reached ~1.5 R_E at some longitudes on 31 October 2003, based on the EUV images from the IMAGE satellite (Baker et al., 2004). To validate this hypothesis, we estimated the minimum L_{PP} based on an empirical model (O'Brien and Moldwin, 2003) using the D_{st} index as input and certainly confirmed the large difference in the estimated minimum L_{PP}. The minimum L_{PP} was 2.51 for the September 2017 storm, whereas in Baker et al. (2004) for the Halloween storm, the minimum L_{PP} was estimated to be 1.82.

4.2. Expansion of the Midlatitude Trough

Figures 4a–4c show the geomagnetic latitude-time plots of the ratio of the difference ATEC from 1800 7 September to 2400 UT 8 September 2017, over the American longitude sectors (magnetic longitude: 199.21°, 215.75°, and 231.89°). The dotted yellow lines in each panel indicate the location of the midlatitude trough minimum determined from the minimum value of the ratio of the difference ATEC. The location of the trough minimum moves equatorward (e.g., Rodger, 2008) in all the longitude sectors after 2200 UT 7 September, corresponding to the storm main phase.

Figure 4d is the two-dimensional ATEC polar map in the Northern Hemisphere with the Altitude Adjusted Corrected GeoMagnetic coordinates at 2340 UT 8 September, corresponding to the time when the Arase observation shows the most deeply eroded plasmasphere. The midlatitude trough is seen in the dusk and postmidnight sectors.

The equatorward movement of the midlatitude trough minimum is qualitatively consistent with the location of the plasmapause observed by Arase. When the storm developed as IMF B_z turned southward and storm time convection expanded, the trough minimum in the American sector moved to the low-latitude regions, and the location was approximately 48° in magnetic latitude at 2340 UT on 8 September, which corresponds to $L = 2.2$. Considering that the equatorward wall of the midlatitude trough corresponds to the plasmapause (e.g., Tsurutani et al., 2004), this result is almost consistent with the Arase electron density profile #4 in Figure 3. The midlatitude trough has been studied as a good indicator of the plasmapause location (Anderson et al., 2008; Yizengaw & Moldwin, 2005) by examining correlations between the plasmapause location obtained by EUV images from the IMAGE spacecraft and the midlatitude trough using tomographic GPS imaging, and the light ion trough identified by using the Defense Meteorological Satellite Program measurements, respectively.

4.3. Penetration of the Convection Electric Field

To understand the physical mechanism that drives equatorward movement of the plasmapause, we investigate storm time response of the electric field, which is the main driver of plasmaspheric dynamics. Figure 5 shows the difference of the north-south component of the geomagnetic field between the low latitude and the dip equator (ΔX) at the American longitudes (top) and the East Asian longitudes (bottom), respectively. The small triangles in the top and bottom panels indicate local noon and midnight, respectively. When the low-latitude magnetometer is located at 6° to 9° away from the dip equator, ΔX is strongly related to the electrojet contribution, which, in turn, is directly related to the eastward electrostatic field that created the electrojet current (e.g., Anderson et al., 2002). Furthermore, ΔX variations have been shown to be quantitatively related with equatorial plasma vertical $\mathbf{E} \times \mathbf{B}$ drift (e.g., Anderson et al., 2002). For example, Figure 2 of Kelley et al. (2003) shows the amazingly remarkable correlation between ΔX and the eastward electric field measured by the Jicamarca incoherent scatter radar, once the daytime conductivity is established. The EEJ variations for both longitude sectors indicate penetration of the high-latitude convection for several hours.

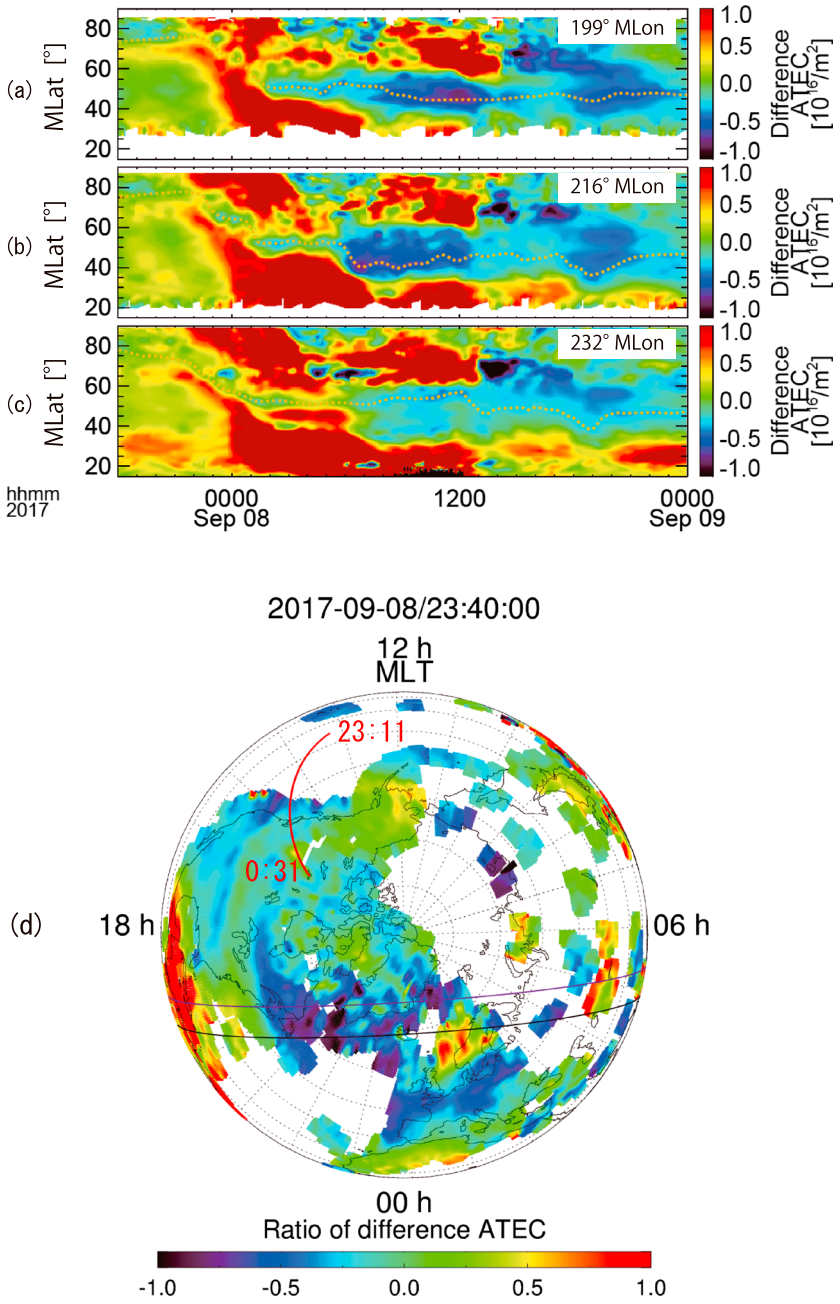

Figure 4. (a–c) The geomagnetic latitude-time plots of the ratio of the difference Absolute Global Navigation Satellite Systems-Total Electron Content (ATEC) at three magnetic longitude (199.21°, 215.75°, and 231.89°) over the American sectors. The dotted yellow lines in each panel indicate the location of the trough minimum determined from the minimum value of the ratio of the difference ATEC, and moves equatorward in all three longitude sectors after 2200 UT. (d) Two-dimensional ATEC polar map in the Northern Hemisphere of the Altitude Adjusted Corrected GeoMagnetic coordinates at 2340 UT on 8 September 2017. The color code indicates a ratio of difference ATEC, corresponding to the time when the Arase observation shows the most deeply eroded plasmasphere. The midlatitude trough is seen in the dusk and postmidnight sectors. The black and purple curves represent the day-night terminator at the heights of 300 and 110 km, respectively. The thick red curve shows the footprint of the Arase spacecraft orbit at the height of 100 km from 2311 UT on 8 September to 0037 UT on 9 September, corresponding to the time range of the electron density profile indicated by #4 in Figure 3. MLT = magnetic local time.

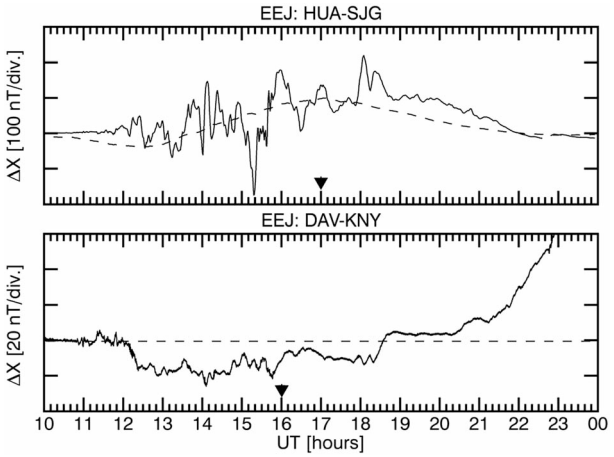

Figure 5. The difference of the north-south (X) component of the geomagnetic field observations between the low latitude and the dip equator (ΔX) at the American longitudes (top) and the East Asian longitudes (bottom), respectively. The solid line (top) shows the difference between Huancayo (HUA) and San Juan (SJG), American longitudes, while the solid line (bottom) shows the difference between Davao (DAV) and Kanoya (KNY), East Asian longitudes from 1000 to 2400 UT of 8 September 2017. The dashed line (top) shows the quiet time reference obtained from 28 August 2017, while the dashed line (bottom) shows a nighttime level for reference. The small triangles in the top and bottom panels indicate local noon and midnight, respectively. The equatorial electrojet (EEJ) variations for both longitude sectors indicate penetration of the high-latitude convection for several hours.

The nightside EEJ in the East Asian longitude sector (Figure 5 bottom) indicates that the penetration of the convection electric field lasted from 1200 to 1800 UT on 8 September 2017. It is surprising that the shielding process (e.g., Jaggi & Wolf, 1973) was ineffective for 6 hr even though it is speculated that the ring current distribution should have become a more symmetric "ring" that creates more effective shielding as more than 12 hr had passed since the first major southward turning at 2300 UT on 7 September. Magnetospheric reconfiguration could have been happening to prevent shielding from being established (e.g., Fejer et al., 1990; Maruyama et al., 2007; see section 5.5).

The dayside EEJ in the American longitude sector (Figure 5 top) shows highly dynamic variation with both positive and negative changes as compared to the quiet time reference. The increase, due to the dynamically varying penetration effect, is imposed on top of the reduction due to the smoothly varying disturbance dynamo effect (e.g., Blanc & Richmond, 1980). The disturbance dynamo electric field is caused by the storm time neutral wind, which generates reversal of the quiet time equatorial zonal electric field (i.e., westward electric field). The neutral wind had enough time to have responded to the high-latitude Joule heating as 13 hr passed since the first major southward turning. The ΔX variation seems to resemble what was reported in Figure 2 in Maruyama et al. (2007) in which the combined effect of both penetration and the disturbance dynamo was taking place in the observed ΔH variation at 1500–2100 UT on 31 March 2001, during the second IMF B_z southward turning.

The cause of the equatorial EEJ variations during storms is attributed to DP2 magnetic field variations (convection) due to IMF (e.g., Nishida, 1968; Kikuchi et al., 1996, 2010), dynamic pressure (Sibeck et al., 1998), and Region 2 field-aligned current enhancement associated with the substorm onset (Ebihara et al., 2014; Fejer et al., 1979; Hashimoto et al., 2011, 2017; Kikuchi et al., 2000). However, it is challenging to quantify the relative contributions of individual effects.

From Figure 5 it can be said that a westward (convection) electric field has penetrated for about 6 hr at least in the nightside ionosphere. The nightside EEJ was an order of magnitude smaller than the dayside EEJ as shown for geomagnetic storms (Tsuji et al., 2012; Wei et al., 2013) and substorms (Hashimoto et al., 2017), which indicates penetration of the electric field to the nightside equatorial ionosphere.

4.4. Numerical Experiments With the IPE Model

Here we demonstrate that the IPE model simulation qualitatively reproduces the observed severe plasmasphere erosion. Figure 6 shows a comparison between the electron density profiles of the two runs: (top) without and (bottom) with enhanced zonal electric field. The profiles are plotted for all 18 different meridional planes in order to see the MLT dependence. The colors of the lines represent the MLT of the meridional planes. The effect of the prompt penetration electric field is not included in the original Weimer model (Weimer, 1996), mainly because the potential is set to zero at the lower boundary at 40° magnetic latitude. The EEJ variations, however, shown in Figure 5, seem to indicate the long-lasting penetration electric field (e.g., Huang et al., 2005). Thus, we increase the zonal electric field in IPE to investigate the impact of the increased zonal electric field on the plasmaspheric profiles and to see whether the model can reproduce the observed deep erosion of the plasmasphere. Figure 7 shows an example of the increased the zonal electric field at MLT = 23.9 hr. (The increase has been achieved by smoothly connecting the field between the values at 56.8° [$L = 3.4$] and 27.1° [$L = 1.3$] magnetic latitude in IPE.) The meridional electric field is kept the same as the default electric field specified by the Weimer model.

The plasmapause is pushed to earthward more severely mostly near the 2400 MLT sector, with the minimum plasmapause at L_P~1.5 in the simulation with the enhanced zonal electric field in Figure 6b (as we expected), while Figure 6a, the default simulation, shows L_P~2.3 near the 2400 MLT sector.

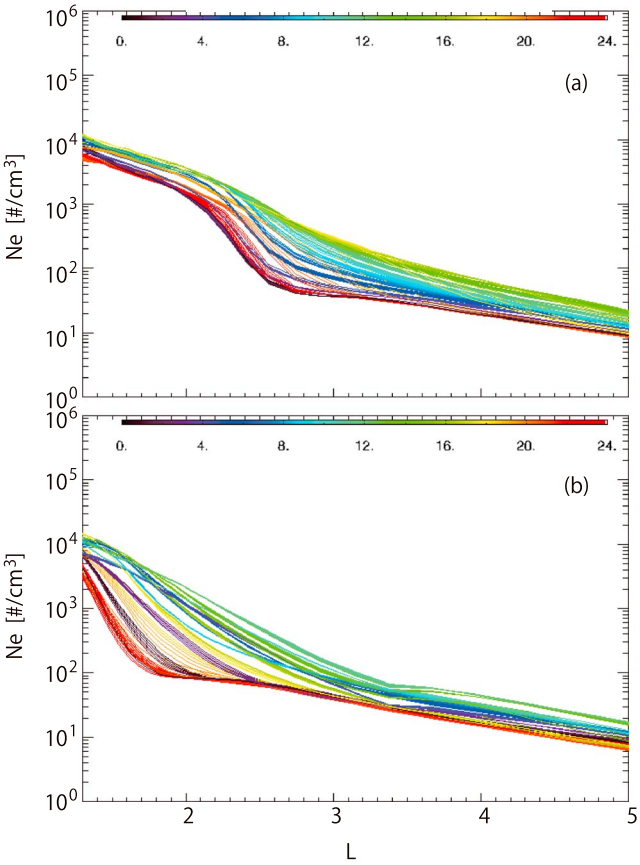

Figure 6. (top) Plasmaspheric electron density profiles obtained by the ionosphere-plasmasphere-electrodynamics simulation as a function of *L*. The color of the curves represents the different magnetic local time (MLT) sectors. The observation period is during the interval of 2248–2400 UT on 8 September 2017. This simulation is with a default setting (without the penetration electric field). (bottom) Plasmaspheric electron density profiles in the same format as the top panel, except that this ionosphere-plasmasphere-electrodynamics simulation is with the penetration electric field. The plasmapause is pushed to earthward more severely mostly near the 2400 MLT sector, with the minimum plasmapause at L_P~1.5 in the simulation with the enhanced zonal electric field in bottom panel, while in top panel, the default simulation shows L_P~2.3 near the 2400 MLT sector.

5. Discussions

5.1. In Situ Observation of Deep Erosion of the Plasmasphere

This is the first observation of the deep erosion of the plasmasphere ($L_{PP} \leq 2$) with the in situ observation of the electron density. The PWE-HFA onboard Arase spacecraft covers a wide frequency range from 10 kHz to 10 MHz. Such wide frequency coverage enables continuous observation of electron density from sparse magnetosphere to dense ionosphere and detection of the plasmapause even if it is during the deep erosion event.

5.2. Comparison With the Empirical Model of the Plasmapause Location

The profiles of electron density shown in Figure 3 are qualitatively consistent with the usual cartoon picture of erosion and refilling of the plasmasphere (e.g., Park, 1973). Here we notice that the cartoon view does not apply except to measurements at a fixed local time or to average measurements over a fixed range of local times. For example, Krall et al. (2017) did a simulation study of plasmasphere erosion in which the authors obtained profiles versus *L* by averaging over the dawn half of the simulated plasmasphere. To minimize the local time effect, we used data from only outbound Arase orbits. As described in section 4.1, all of the plasmapause crossings in this study are inside the range of MLT = 13.1–16.3.

We compare our results with the plasmapause location predicted by the experimental model of O'Brien and Moldwin (2003). $AE_{\ \max}$ in the past 36–0 hr, $D_{st\ \min}$ (SYM-H $_{\min}$) in the past 36–2 hr, and $K_{p\ \max}$ in the past 36–2 hr for the period of 2000–2400 UT on 8 September 2017 were, respectively, 2,677 nT, −146 nT, and 8+, and the plasmapause location was predicted at 2.06, 2.51, and 1.79 R_E by using these values. Only the K_p model provided results that corresponded with our observations. In the predictions using D_{st} and *AE*, the plasmapause locations did not reach deep inside as much as the observations.

O'Brien and Moldwin (2003) argued that the *AE* or D_{st} indices provided better model of the plasmapause location than K_p. This is inconsistent with our results. *AE* and D_{st}, respectively, reflect the auroral electrojet and ring current. At least in the September 2017 storm event, the influence of these current systems apparently has not been able to quantitatively explain the deep erosion of the plasmasphere.

In this storm event, the plasmapause location predicted by the O'Brien and Moldwin model (2003) is scattered because K_p was large, despite the minor decrease in SYM-H. Since our observation results best matched the results of the K_p model with the smallest L_{PP}, perhaps the true scale of the magnitude of the convection electric field (Thomsen, 2004), which directly affects the plasmapause location, should be considered substantially large as K_p indicates. In this storm event, the SYM-H index seems not to have scaled magnitude of the convection electric field well.

5.3. Time Lag of the Plasmaspheric Erosion

As shown in Figure 1, the cross polar cap potential drop had two major increases beginning around 2300 UT on 7 September and 1200 UT on 8 September 2017, whereas Figure 3 shows that the erosion of the plasmasphere gradually progressed from 1800 on 7 September to the end of 8 September and the most deeply eroded plasmasphere was observed at 2300 UT on 8 September. In other words, there was half a day to one day of time lag from cross polar cap potential drop increases to the smallest plasmasphere observed. This time lag will be qualitatively understood by a general convection-based model.

Development of the convection electric field causes the sunward motion of the plasma, which makes the inward motion of the nightside plasmapause, whereas in the dayside, the plasmasphere bulges sunward,

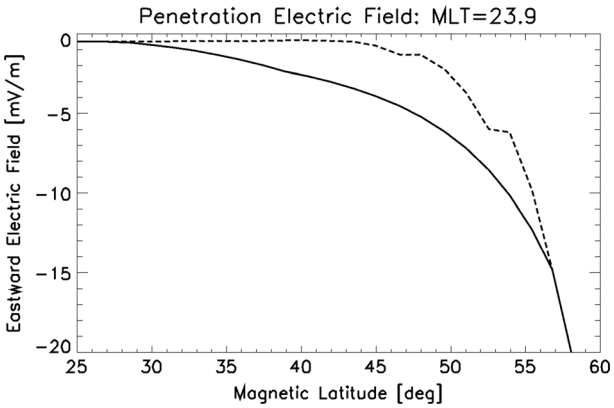

Figure 7. Latitude profile of the zonal electric field (mV/m) used in the ionosphere-plasmasphere-electrodynamics simulations with the default setting (dashed line) and with the increased electric field setting (solid line). MLT = magnetic local time.

forming a wide range of plumes. When the convection subsequently decreases, these structures start to rotate eastward, causing plume narrowing and a small plasmapause radius, which also moves eastward (e.g., Spasojević et al., 2003). In order for the dayside plasmasphere to erode, it is necessary to wait for the eroded plasmasphere in the nightside to rotate eastward and reach dayside.

In this study, only the outbound Arase data were analyzed, so all of the profiles shown in Figure 3 are from the dayside magnetosphere. The Arase position was 1300 MLT, when the spacecraft passed L=1.6–1.7 in orbit #4. According to Bandić et al. (2016), there were 7 hr of time lag for the effect of erosion to reach to 1200 MLT. Our results qualitatively agree with this result, and this suggests that the time history of the electric field experienced by each flux tube is an important factor determining the deformation of the plasmasphere.

5.4. Shape of the Plasmapause

Interestingly, the electron density structure outside the plasmapause was totally different between profiles #3 and #4 in Figure 3 despite of the almost same MLT and the only 8 hr of time difference. In $L \geq 3$ of #3 profile, the density showed perturbations, in other words, increase and decrease of density. These perturbations are often observed by Arase (Kazama et al., 2018). On the other hand, in #4 profile, it had a smooth density structure except for an increase in the density in L = 3.4–4.3 (probably, it is the plume). Similar density variations over L of both #3 and #4 profiles have also been recorded by the Electric and Magnetic Field Instrument Suite and Integrated Science instrumentation suite (Kletzing et al., 2013) of the Van Allen Probes (Mauk et al., 2013; not shown).

How is such density perturbations made? Since the IPE model does not reproduce this structure, we cannot fully explain this, but time history and/or the special structure of the convection field may be important. It may be possible to make such a structure that the motion of the plasma due to the superimposition of the corotation and convection, which repetitive increase and decrease. Furthermore, Borovsky and Denton (2008) suggested some possible causes of lumpiness of plumes including (1) $\mathbf{E} \times \mathbf{B}$ gradient—drift instability, (2) velocity shear, and (3) high Reynolds-number turbulent flows, based on statistical analysis of measurements by the Los Alamos Magnetospheric Plasma Analyzer (MPA) in geosynchronous orbit.

5.5. Long-Lasting Disturbance Electric Field Under a Dynamically Changing Magnetosphere

The long-lasting disturbance electric field in Figures 5 and 6 seems to suggest that the shielding time constant is longer than what we would have expected from conventional understanding. In shielding, the Region 2 field-aligned (Birkeland) currents associated with pressure gradients of the partial ring current near the inner edge of the plasma sheet produce an eastward electric field by closing through the ionosphere (Jaggi & Wolf, 1973). The resultant dusk-to-dawn electric field is responsible for shielding the inner magnetosphere and midlatitude and low-latitude ionosphere from the full effect of the global dawn-to-dusk solar wind-driven convection field. The net electric field inside (equatorward) of the Region 2 current is greatly reduced and becomes small once the shielding has been established. The shielding time scale is usually ~1 hr since the response time of the magnetosphere is about 0.5–1 hr (Jaggi & Wolf, 1973). However, the long-lasting penetration of the convection field inferred by the EEJ in Figure 5 and the deep erosion of the plasmasphere in Figure 6 seem to indicate that the "undershielding" effect lasted for several hours, even 12 hr, after the storm commencement. In recent years, Huang et al. (2005, 2006) pointed out possible evidence for longer-lasting penetration of magnetospheric electric fields. It is important to note that most of this evidence is usually related to long-lasting geomagnetic disturbances that may not resemble the idealized changes in the convection strength leading to the "disrupt and restore" of the magnetosphere inside idealized model simulations in previous shielding studies. Furthermore, Maruyama et al. (2007) addressed the question, "can long-lasting disturbance electric field be attributed to the penetration mechanism?", by using physics-based models of the magnetosphere-ionosphere-thermosphere system. The penetration effect can have a longer lifetime when the IMF B_z is large and negative as compared to the historical picture of

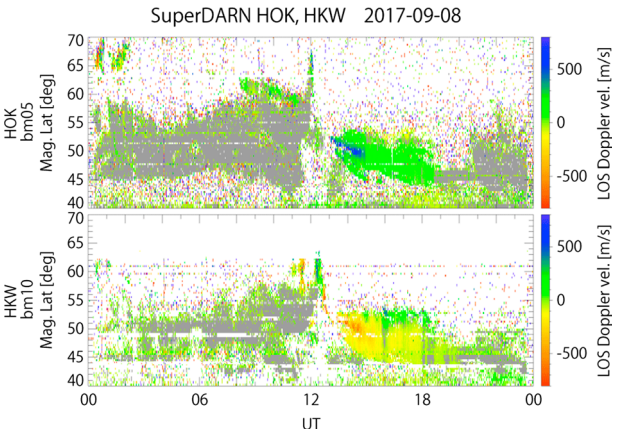

Figure 8. The range-time-intensity plots of the line-of-sight Doppler velocities (positive toward radars) obtained by the Super Dual Auroral Radar Network (SuperDARN) Hokkaido East (top, beam 5) and West (bottom, beam 10) radars on 8 September 2017. Strong positive (negative) velocity regions can be identified between 1300 and 1500 UT around 50° magnetic latitude. Beam 5 of the east radar and beam 10 of the west radar roughly direct the magnetic northeast and the magnetic northwest, respectively; thus, the strong velocity can be interpreted as a strong westward flow. The usual velocity flow with the same direction continued until 2000 UT at 44–53° magnetic latitude. Thus, we confirm that the enhanced northward electric field penetrated to <50° magnetic latitude, a much lower latitude than usual, even if we consider relatively high negative D_{st} values.

prompt penetration. It is caused by ineffective shielding due to the magnetospheric reconfiguration (Fejer et al., 1990). The magnetospheric reconfiguration process results from the constant stretching of the magnetotail mainly during the early main phase of the storm. The magnitude and lifetime of the penetration electric field seem to be controlled by the rate and duration of stretching of the magnetic field. Enhanced reconnection at the dayside magnetopause results in constant transfer of magnetic flux to the lobes of the magnetotail, causing stretching of nightside plasma sheet magnetic field lines. Furthermore, Lei et al. (2018) reported that the observed long-lasting positive response in daytime TEC at midlatitude on 8 September 2017 was also caused by the penetration electric field. Our study suggests that further investigations are needed to reevaluate the shielding time scale in a more realistic geospace environment.

5.6. Possible Cause of the Discrepancy Between IPE Simulations and Observations

The most distinct plasmapause in the plasmasphere electron density profile in the IPE model simulations in Figure 6 was located near the 2400 MLT sector (red and dark blue), while the actual Arase orbit was located in the dayside MLT when it crossed the plasmapause at $L = 1.6$. The MLT variation of the electron density profile was not captured very well mainly because the enhancement in the meridional electric field was not included (i.e., meridional electric field was the same as in the Weimer, 1996, model) in the IPE simulations shown in Figure 6. The azimuthal plasma transport generated by the meridional electric field plays an important role in transporting the nighttime plasma toward sunward (e.g., Goldstein, 2006). Furthermore, the disturbance dynamo electric field was not included in the IPE simulations. Figure 5 seems to indicate that the disturbance dynamo process played a role in the observed EEJ during the second cross polar cap potential drop enhancement at ~1300 UT on 8 September 2017. The observed EEJ variation in the American longitude sector resembles that shown in Figure 2 in Maruyama et al. (2007). The simulations based on the combined first-principles CTIP-RCM model suggests that the disturbance dynamo effect reduces the daytime upward $\mathbf{E} \times \mathbf{B}$ drift while the simultaneous prompt penetration adds the highly variable fluctuation on top of the smoothly reduced drift. Furthermore, the storm time midlatitude zonal drift caused by the disturbance dynamo process is mostly westward (e.g., Galvan et al., 2010), which could have impacted the observed MLT variation of the plasmasphere.

IPE simulations were not able to capture the observed plumes in profile #4. This could be due to lack of fine structures in the electric field distributions used in the simulations. Furthermore, the current version of the IPE model did not have enough spatial resolution in the L direction in order to resolve the fine structures (L direction resolution is $\Delta L = 0.079$ at $L = 1.67$ in the plasmasphere). The IPE simulations did not include other processes, such as Subauroral Polarization Streams and substorms, that could have contributed to the fine structures in the electric field. For example, high-frequency variation in ΔX in the American longitude sector (HUA-SJG) at night shown in Figure 5 is most likely caused by substorms. Both AL variations and Pi2 seem to indicate some substorm activities (plots not shown). The enhanced westward flow in the subauroral region associated with Subauroral Polarization Streams is investigated by the SuperDARN Hokkaido radars. Figure 8 shows the range-time-intensity plots of the line-of-sight Doppler velocities (positive toward the radars) along beam 5 of the Hokkaido East radar (top) and beam 10 of the Hokkaido West radar (bottom). Strong positive (negative) velocity regions can be identified between 1300 and 1500 UT around 50° magnetic latitude. Beam 5 of the east radar and beam 10 of the west radar roughly direct the magnetic northeast and the magnetic northwest, respectively; thus, the strong velocity can be interpreted as a strong westward flow. The usual velocity flow with the same direction continued until 2000 UT at 44–53° magnetic latitude. Thus, we confirm that the enhanced northward electric field penetrated to <50° magnetic latitude, a much lower latitude than usual, even if we consider relatively high negative D_{st} values (Kataoka et al., 2009; Nagano et al., 2015).

A more accurate prediction of the time history of the plasmaspheric electric field distribution will be needed to improve the prediction of plasmapause locations changing dynamically in time and space. The use of the electric field calculated from global magnetospheric MHD models coupled to a ring current model would be an ideal next step of our study.

5.7. Importance in Establishing Space Weather Forecasting

Cross-energy coupling via wave-particle interactions is an important concept to understand the plasma environment in the inner magnetosphere [e.g., Miyoshi, Shinohara, et al., 2018]. Despite the fact that the plasmasphere consists of the lowest-energy plasma in the inner magnetosphere, it has a strong influence on the dynamics of the radiation belt. Several mechanisms have been suggested to interpret how the plasmasphere affects the dynamics of the radiation belt (e.g., Degeling et al., 2007; Horne et al., 2005; Miyoshi et al., 2003, 2013), and many of those are based on the ideas that plasma waves generated on or around the plasmapause diffuse or accelerate the radiation belt particles. In that sense, prediction of the location of the plasmapause is an important challenge for the establishment of space weather forecasting.

This study introduced deep erosion of the plasmasphere in a storm event having a moderate (−146 nT) SYM-H $_{min}$. In such a case, the effect on the radiation belt can also occur in the magnetosphere far inside those usually considered. These are important implications for future space weather forecasts, especially prediction of the development of the radiation belt during magnetic storms.

6. Conclusions

Our paper reports that the severe depletion of the plasmasphere was observed by the PWE instrument onboard the ERG/Arase satellite on 2300 UT 8 September 2017 during the recovery phase of the September 2017 storm. The degree of the severity is much more than what would be expected from the relatively nominal value of the SYM-H $_{min}$ (−146 nT). For example, Baker et al. (2004) used IMAGE EUV data and reported that the plasmapause radius was inside 2 R_E and at some longitudes was at 1.5 R_E during the 2003 Halloween storm. However, $D_{st\ min}$ was −383 nT during this storm, and the expected L_{PP} was comparable to the observations.

We also report that the midlatitude ionospheric trough shown in the ratio of difference ATEC widely expanded equatorward and reached ~48° in the dusk side ionosphere. The nightside EEJ in the East Asian longitude sector indicates that the penetration of the convection electric field lasted from 1200 to 1800 UT on 8 September. It is surprising that the shielding process seems to be ineffective even though more than 12 hr had passed since the first major southward turning at 2300 UT on 7 September. The Hokkaido East and West radars also registered enhancement of the northward electric field to penetrate to unusually low latitudes (<50° magnetic latitude).

We attempted to find a possible explanation for the observed severe depletion by using both observational evidence and numerical simulations. The IPE model simulations were run in two modes: (i) the default setting run where the potential was set to 0 at the lower-latitude boundary as given by the Weimer (1996) model and (ii) the penetration electric field run where the zonal electric field was artificially increased in the middle latitudes. Only the penetrated electric field run reproduced the severe plasmasphere erosion. Our results suggest that the middle-latitude electric field penetrated from the high-latitude storm time convection that lasted for several hours can explain such a degree of severity.

Our observation is the first report of such a deeply eroded plasmasphere using in situ observation of electron density in the magnetosphere. Arase observation, especially spectrograms of plasma waves in a wide (10 kHz to 10 MHz) frequency range, is a strong tool for research on deep erosion of the plasmasphere. The next questions arise. If the convection electric field gets stronger, will the corotation region become infinitely small, or could there be any low-altitude limit? If so, what controls the limitation? An interesting theme and a future subject.

Acknowledgments
This work was supported by JSPS KAKENHI Grants 15H05815, 15H05747, and 16H04057. Science data of the ERG (Arase) satellite were obtained from the ERG Science Center operated by ISAS/JAXA and ISEE/Nagoya University, Japan (https://ergsc.isee.nagoya-u.ac.jp/index.shtml.en). The present study analyzed the PWE-HFA v03.00, MGF v01.00, and orbit v01 data. The solar wind parameters are obtained from the NASA OMNI website (https://omniweb.gsfc.nasa.gov/). We acknowledge use of NASA/GSFC's Space Physics Data Facility's OMNIWeb service and OMNI data. The GNSS data collection and processing were performed with the NICT Science Cloud. The Receiver Independent Exchange Format (RINEX) data for the GNSS-TEC processing are provided by the following organizations: UNAVCO (ftp://data-out.unavco.org), DGRSDUT (http://gnss1.tudelft.nl), Arecibo Observatory (http://www.naic.edu), CDDIS (ftp://cddis.gsfc.nasa.gov), CHAIN (ftp://chain.physics.unb.ca), CORS (ftp://www.ngs.noaa.gov), GDAF (ftp://geo-daf.mt.asi.it), BKG (ftp://igs.bkg.bund.de), IGS (ftp://rgpdata.ign.fr), EUOLG (ftp://olggps.oeaw.ac.at), Geoscience Australia (ftp://ftp.ga.gov.au), IGSIGN (ftp://igs.ensg.ign.fr), KASI (ftp://nfs.kasi.re.kr), PNGA (http://www.geodesy.cwu.edu), IBGE (ftp://geoftp.ibge.gov.br), RGCL (ftp://ftp.itacyl.es), TNG (ftp://196.15.132.3), SOPAC (ftp://garner.ucsd.edu), NRC (ftp://wcda.pgc.nrcan.gc.ca), GEONET (ftp://163.42.5.1), HRAO (ftp://geoid.hartrao.ac.za), GRN (ftp://rinex.smartnetna.com), GNNZ (ftp://ftp.geonet.org.nz), RENAG (ftp://renag.unice.fr), SONEL (ftp://ftp.sonel.org), FRDN (ftp://www.crs.inogs.it), LINZ (ftp://apps.linz.govt.nz), ROB (ftp://gnss.oma.be), GOP (ftp://ftp.pecny.cz), RGE (ftp://62.99.86.141), RGNA (ftp://geodesia.inegi.org.mx), CENAT (ftp://www.cenat.ac.cr), INGV (ftp://bancadati2.gm.ingv.it), REP (ftp://158.49.61.10), SWSBM (ftp://ftp-out.sws.bom.gov.au), CORS (ftp://meristemum.carm.es), AFREF (ftp://ftp.afrefdata.org), WHU (ftp://igs.gnsswhu.cn), TLALOCNET (ftp://tlalocnet.udg.mx), NCEDC (ftp://www.ncedc.org), ODT (ftp://ftp.odot.state.or.us), SWEPOS (ftp://ftp.swepos-data.lm.se), EUREF (ftp://www.epncb.oma.be), IGG (ftp://ftp.glonass-iac.ru), SUGAUR (ftp://eos.ntu.edu.sg), NMA (ftp://ftp.statkart.no), NERC (ftp://128.243.138.204), and ERGNSS (ftp://ftp.geodesia.ign.es). The results presented in this paper rely on the data collected at Huancayo, San Juan, and Kanoya from INTERMAGNET and Davao from MAGDAS. The

References

Akmaev, R. A., Fuller-Rowell, T. J., Wu, F., Forbes, J. M., Zhang, X., Anghel, A. F., et al. (2008). Tidal variability in the lower thermosphere: Comparison of Whole Atmosphere Model (WAM) simulations with observations from TIMED. *Geophysical Research Letters*, *35*, L03810. https://doi.org/10.1029/2007GL032584

INTERMAGNET data are obtained through the INTERMAGNET website (hhttp://www.intermagnet.org/index.html). We thank the host institutes for supporting their operation and INTERMAGNET for promoting high standards of magnetic observatory practice (www.intermagnet.org). The MAGDAS data were obtained from the International Center for Space Weather Science and Education (ICSWSE), Kyushu University, Fukuoka, Japan. A. Yoshikawa, the PI of the MAGDAS project, was supported by MEXT/JSPS KAKENHI Grant JP15H05815. The MAGDAS data used in this study are given in the supporting information of this paper. SuperDARN is a collection of radars funded by the national scientific funding agencies of Australia, Canada, China, France, Italy, Japan, Norway, South Africa, United Kingdom, and the United States. The SuperDARN Hokkaido radar data in the CDF format are provided by ERG Science Center, Nagoya University (https://ergsc.isee.nagoya-u.ac.jp/data_info/index.shtml.en). The operation of SuperDARN Hokkaido East and West radar is supported by Special Funds for Education and Research (Energy Transport Processes in Geospace); the Inter-university Upper atmosphere Global Observation Network (IUGONET) project of the Ministry of Education, Culture, Sports, Science and Technology of Japan; and MEXT/JSPS KAKENHI Grants 16H06286 and 18KK0099. The work of T. H. and Y. M. was partly done at the ERG Science Center operated by JAXA/ISAS and ISEE, Nagoya University, Japan. This work was supported by NASA grants (NNX16AB83G, NNX15AI91G, 80NSSC17K0720, 80NSSC17K0718, 80NSSC19K0084, 80NSSC19K0277), NSF grants (AGS-1452298, AGS-1552248), and AFOSR FA9550-18-1-0483.

Anderson, D. N., Anghel, A., Yumoto, K., Ishitsuka, M., & Kudeki, E. (2002). Estimating daytime vertical **E** × **B** drift velocities in the equatorial *F* region using ground-based magnetometer observations. *Geophysical Research Letters*, *29*(12), 1596. https://doi.org/10.1029/2001GL014562

Anderson, P. C., Johnston, W. R., & Goldstein, J. (2008). Observations of the ionospheric projection of the plasmapause. *Geophysical Research Letters*, *35*, L15110. https://doi.org/10.1029/2008GL033978

Baker, D. N., Kanekal, S. G., Li, X., Monk, S. P., Goldstein, J., & Burch, J. L. (2004). An extreme distortion of the Van Allen belt arising from the 'Halloween' solar storm in 2003. *Nature*, *432*(7019), 878–881. https://doi.org/10.1038/nature03116

Baker, K. B., & Wing, S. (1989). A new coordinate system for conjugate studies at high latitudes. *Journal of Geophysical Research*, *94*(A7), 9139–9143. https://doi.org/10.1029/JA094iA07p09139

Bandić, M., Verbanac, G., Moldwin, M. B., Pierrard, V., & Piredda, G. (2016). MLT dependence in the relationship between plasmapause, solar wind, and geomagnetic activity based on CRRES: 1990–1991. *Journal of Geophysical Research: Space Physics*, *121*, 4397–4408. https://doi.org/10.1002/2015JA022278

Blanc, M., & Richmond, A. D. (1980). The ionospheric disturbance dynamo. *Journal of Geophysical Research*, *85*(A4), 1669–1686. https://doi.org/10.1029/JA085iA04p01669

Borovsky, J. E. (2014). Feedback of the magnetosphere. *Science*, *343*(6175), 1086–1087. https://doi.org/10.1126/science.1250590

Borovsky, J. E., & Denton, M. H. (2008). A statistical look at plasmaspheric drainage plumes. *Journal of Geophysical Research*, *113*, A09221. https://doi.org/10.1029/2007JA012994

Boyle, C. B., Reiff, P. H., & Hairston, M. R. (1997). Empirical polar cap potentials. *Journal of Geophysical Research*, *102*(A1), 111–125. https://doi.org/10.1029/96JA01742

Carpenter, D. L., & Anderson, R. R. (1992). An ISEE/whistler model of equatorial electron density in the magnetosphere. *Journal of Geophysical Research*, *97*(A2), 1097–1108. https://doi.org/10.1029/91JA01548

Carpenter, D. L., & Park, C. G. (1973). What ionospheric workers should know about the plasmapause-plasmasphere. *Reviews of Geophysics*, *11*(1), 133–154. https://doi.org/10.1029/RG011i001p00133

Chappell, C. R., Harris, K. K., & Sharp, G. W. (1970). A study of the influence of magnetic activity on the location of the plasmapause as measured by OGO 5. *Journal of Geophysical Research*, *75*(1), 50–56. https://doi.org/10.1029/JA075i001p00050

Degeling, A. W., Rankin, R., Kabin, K., Marchand, R., & Mann, I. R. (2007). The effect of ULF compressional modes and field line resonances on relativistic electron dynamics. *Planetary and Space Science*, *55*(6), 731–742. https://doi.org/10.1016/j.pss.2006.04.039

Ebihara, Y., Tanaka, T., & Kikuchi, T. (2014). Counter equatorial electrojet and overshielding after substorm onset: Global MHD simulation study. *Journal of Geophysical Research: Space Physics*, *119*, 7281–7296. https://doi.org/10.1002/2014JA020065

Fejer, B. G., Gonzales, C. A., Farley, D. T., & Kelley, M. C. (1979). Equatorial electric fields during magnetically disturbed conditions: 1. The effect of the interplanetary magnetic field. *Journal of Geophysical Research*, *84*(A10), 5797–5802. https://doi.org/10.1029/JA084iA10p05797

Fejer, B. G., Spiro, R. W., Wolf, R. A., & Foster, J. C. (1990). Latitudinal variation of perturbation electric fields during magnetically disturbed periods: 1986 SUNDIAL observations and model results. *Annales Geophysicae*, *8*(6), 441–454.

Fuller-Rowell, T. J., Akmaev, R. A., Wu, F., Anghel, A., Maruyama, N., Anderson, D. N., et al. (2008). Impact of terrestrial weather on the upper atmosphere. *Geophysical Research Letters*, *35*, L09808. https://doi.org/10.1029/2007GL032911

Fuller-Rowell, T. J., & Evans, D. S. (1987). Height-integrated Pedersen and Hall conductivity patterns inferred from the TIROS-NOAA satellite data. *Journal of Geophysical Research*, *92*(A7), 7606–7618. https://doi.org/10.1029/JA092iA07p07606

Galvan, D. A., Moldwin, M. B., Sandel, B. R., & Crowley, G. (2010). On the causes of plasmaspheric rotation variability: IMAGE EUV observations. *Journal of Geophysical Research*, *115*, A01214. https://doi.org/10.1029/2009JA014321

Goldstein, J. (2006). Plasmasphere response: Tutorial and review of recent imaging results. *Space Science Reviews*, *124*(1-4), 203–216. https://doi.org/10.1007/s11214-006-9105-y

Goldstein, J., De Pascuale, S., Kletzing, C., Kurth, W., Genestreti, K. J., Skoug, R. M., et al. (2014). Simulation of Van Allen Probes plasmapause encounters. *Journal of Geophysical Research: Space Physics*, *119*, 7464–7484. https://doi.org/10.1002/2014JA020252

Greenwald, R. A., Baker, K. B., Dudeney, J. R., Pinnock, M., Jones, T. B., Thomas, E. C., et al. (1995). DARN/SUPERDARN: A global view of the dynamics of high-latitude convection. *Space Science Reviews*, *71*(1-4), 761–796. https://doi.org/10.1007/BF00751350

Hairston, M. R., Drake, K. A., & Skoug, R. (2005). Saturation of the ionospheric polar cap potential during the October-November 2003 superstorms. *Journal of Geophysical Research*, *110*, A09S26. https://doi.org/10.1029/2004JA010864

Hairston, M. R., Hill, T. W., & Heelis, R. A. (2003). Observed saturation of the ionospheric potential during the 31 March 2001 storm. *Geophysical Research Letters*, *30*(6), 1325. https://doi.org/10.1029/2002GL015894

Hashimoto, K. K., Kikuchi, T., Tomizawa, I., & Nagatsuma, T. (2017). Substorm overshielding electric field at low latitude on the nightside as observed by the HF Doppler Sounder and magnetometers. *Journal of Geophysical Research: Space Physics*, *122*, 10,851–10,863. https://doi.org/10.1002/2017JA024329

Hashimoto, K. K., Kikuchi, T., Watari, S., & Abdu, M. A. (2011). Polar-equatorial ionospheric currents driven by the region 2 field-aligned currents at the onset of substorms. *Journal of Geophysical Research*, *116*, A09217. https://doi.org/10.1029/2011JA016442

Hedin, A. E., Fleming, E. L., Manson, A. H., Schmidlin, F. J., Avery, S. K., Clark, R. R., et al. (1996). Empirical wind model for the upper, middle and lower atmosphere. *Journal of Atmosphere and Terrestrial Physics*, *58*(13), 1421–1447. https://doi.org/10.1016/0021-9169(95)00122-0

Horne, R. B., Thorne, R. M., Glauert, S. A., Albert, J. M., Meredith, N. P., & Anderson, R. R. (2005). Timescale for radiation belt electron acceleration by whistler mode chorus waves. *Journal of Geophysical Research*, *110*, A03225. https://doi.org/10.1029/2004JA010811

Huang, C.-S., Foster, J. C., & Kelley, M. C. (2005). Long-duration penetration of the interplanetary electric field to the low-latitude ionosphere during the main phase of magnetic storms. *Journal of Geophysical Research*, *110*, A11309. https://doi.org/10.1029/2005JA011202

Huang, C.-S., Sazykin, S., Chao, J., Maruyama, N., & Kelley, M. C. (2006). Penetration electric fields: Efficiency and characteristic time scale. *Journal of Atmospheric and Solar-Terrestrial Physics*, *69*(10), 1135–1146. https://doi.org/10.1016/j.jastp.2006.08.016

Jaggi, R. K., & Wolf, R. A. (1973). Self-consistent calculation of the motion of a sheet of ions in the magnetosphere. *Journal of Geophysical Research*, *78*(16), 2852–2866. https://doi.org/10.1029/JA078i016p02852

Kasahara, Y., Kasaba, Y., Kojima, H., Yagitani, S., Ishisaka, K., Kumamoto, A., et al. (2018). The Plasma Wave Experiment (PWE) on board the Arase (ERG) satellite. *Earth, Planets and Space*, *70*(1), 86. https://doi.org/10.1186/s40623-018-0842-4

Kataoka, R., Hosokawa, K., Nishitani, N., & Miyoshi, Y. (2009). SuperDARN Hokkaido radar observation of westward flow enhancement in subauroral latitudes. *Annales Geophysicae*, *27*(4), 1695–1699. https://doi.org/10.5194/angeo-27-1695-2009

Kazama, Y., Kojima, H., Miyoshi, Y., Kasahara, Y., Usui, H., Wang, B.-J., et al. (2018). Density depletions associated with enhancements of electron cyclotron harmonic emissions: An ERG observation. *Geophysical Research Letters*, *45*, 10,075–10,083. https://doi.org/10.1029/2018GL080117

Kelley, M. C., Makela, J. J., Chau, J. L., & Nicolls, M. J. (2003). Penetration of the solar wind electric field into the magnetosphere/ionosphere system. *Geophysical Research Letters*, *30*(4), 1158. https://doi.org/10.1029/2002GL016321

Kikuchi, T., Ebihara, Y., Hashimoto, K. K., Kataoka, R., Hori, T., Watari, S., & Nishitani, N. (2010). Penetration of the convection and overshielding electric fields to the equatorial ionosphere during a quasiperiodic DP 2 geomagnetic fluctuation event. *Journal of Geophysical Research*, *115*, A05209. https://doi.org/10.1029/2008JA013948

Kikuchi, T., Lühr, H., Kitamura, T., Saka, O., & Schlegel, K. (1996). Direct penetration of the polar electric field to the equator during a DP 2 event as detected by the auroral and equatorial magnetometer chains and the EISCAT radar. *Journal of Geophysical Research*, *101*(A8), 17,161–17,173. https://doi.org/10.1029/96JA01299

Kikuchi, T., Lühr, H., Schlegel, K., Tachihara, H., Shinohara, M., & Kitamura, T.-I. (2000). Penetration of auroral electric fields to the equator during a substorm. *Journal of Geophysical Research*, *105*(A10), 23,251–23,261. https://doi.org/10.1029/2000JA900016

Kletzing, C. A., Kurth, W. S., Acuna, M., MacDowall, R. J., Torbert, R. B., Averkamp, T., et al. (2013). The Electric and Magnetic Field Instrument Suite and Integrated Science (EMFISIS) on RBSP. *Space Science Reviews*, *179*(1-4), 127–181. https://doi.org/10.1007/s11214-013-9993-6

Krall, J., Huba, J. D., & Sazykin, S. (2017). Erosion of the plasmasphere during a storm. *Journal of Geophysical Research: Space Physics*, *122*, 9320–9328. https://doi.org/10.1002/2017JA024450

Kumamoto, A., Tsuchiya, F., Kasahara, Y., Kasaba, Y., Kojima, H., Yagitani, S., et al. (2018). High Frequency Analyzer (HFA) of Plasma Wave Experiment (PWE) onboard the Arase spacecraft. *Earth, Planets and Space*, *70*(82). https://doi.org/10.1186/s40623-018-0854-0

Lei, J., Huang, F., Chen, X., Zhong, J., Ren, D., Wang, W., et al. (2018). Was magnetic storm the only driver of the long-duration enhancements of daytime total electron content in the Asian-Australian sector between 7 and 12 September 2017? *Journal of Geophysical Research: Space Physics*, *123*, 3217–3232. https://doi.org/10.1029/2017JA025166

Li, X., Baker, D. N., O'Brien, T. P., Xie, L., & Zong, Q. G. (2006). Correlation between the inner edge of outer radiation belt electrons and the innermost plasmapause location. *Geophysical Research Letters*, *33*, L14107. https://doi.org/10.1029/2006GL026294

Maruyama, N., Millward, G., Oehmke, B., Deluca, C., Montuoro, R., Fang, T.-W., et al. (2017). Evaluating the impact of whole atmosphere coupling on storm time response in ionosphere and plasmasphere. Fall AGU meeting, New Orleans, LA, USA

Maruyama, N., Sazykin, S., Spiro, R. W., Anderson, D., Anghel, A., Wolf, R. A., et al. (2007). Modeling storm-time electrodynamics of the low latitude ionosphere-thermosphere system: Can long lasting disturbance electric fields be accounted for? *Journal of Atmosphere and Solar-Terrestrial Physics*, *69*(10–11), 1182–1199. https://doi.org/10.1016/j.jastp.2006.08.020

Maruyama, N., Sun, Y.-Y., Richards, P. G., Middlecoff, J., Fang, T.-W., Fuller-Rowell, T. J., et al. (2016). A new source of the midlatitude ionospheric peak density structure revealed by a new Ionosphere-Plasmasphere model. *Geophysical Research Letters*, *43*, 2429–2435. https://doi.org/10.1002/2015GL067312

Matsuoka, A., Teramoto, M., Nomura, R., Nosé, M., Fujimoto, A., Tanaka, Y., et al. (2018). The ARASE (ERG) magnetic field investigation. *Earth, Planets and Space*, *70*, 43. https://doi.org/10.1186/s40623-018-0800-1

Mauk, B. H., Fox, N. J., Kanekal, S. G., Kessel, R. L., Sibeck, D. G., & Ukhorskiy, A. (2013). Science objectives and rationale for the Radiation Belt Storm Probes Mission. *Space Science Reviews*, *179*(1-4), 3–27. https://doi.org/10.1007/s11214-012-9908-y

Maus, S., Macmillan, S., Chernova, T., Choi, S., Dater, D., Golovkov, V., et al. (2005). The 10th-generation international geomagnetic reference field. *Geophysical Journal International*, *161*(16), 561–565. https://doi.org/10.1029/2005EO160006

McIlwain, C. E. (1961). Coordinates for mapping the distribution of magnetically trapped particles. *Journal of Geophysical Research*, *66*(11), 3681–3691. https://doi.org/10.1029/JZ066i011p03681

Millholland, S., Maruyama, N., Maute, A., Goncharenko, L., Burns, A., Richards, P., et al.. (2013). Modeling sudden stratospheric warming events using the Ionosphere-Plasmasphere-Electrodynamics (IPE) Model. Presented at American Geophysical Union Fall meeting, December 8–13, San Francisco, CA.

Miyoshi, Y., Hori, T., Shoji, M., Teramoto, M., Chang, T.-F., Segawa, T., et al. (2018). The ERG Science Center. *Earth, Planets and Space*, *70*(1), 96. https://doi.org/10.1186/s40623-018-0867-8

Miyoshi, Y., Kataoka, R., Kasahara, Y., Kumamoto, A., Nagai, T., & Thomsen, M. (2013). High-speed solar wind with southward interplanetary magnetic field causes relativistic electron flux enhancement of the outer radiation belt via enhanced condition of whistler waves. *Geophysical Research Letters*, *40*, 4520–4525. https://doi.org/10.1002/grl.50916

Miyoshi, Y., Morioka, A., Obara, T., Misawa, H., Nagai, T., & Kasahara, Y. (2003). Rebuilding process of the outer radiation belt during the November 3, 1993, magnetic storm - NOAA and EXOS-D observations. *Journal of Geophysical Research*, *108*(A1), 1004. https://doi.org/10.1029/2001JA007542

Miyoshi, Y., Shinohara, I., Takashima, T., Asamura, K., Higashio, N., Mitani, T., et al. (2018). Geospace Exploration Project ERG. *Earth, Planets and Space*, *70*(1), 101. https://doi.org/10.1186/s40623-018-0862-0

Moldwin, M. B., Downward, L., Rassoul, H. K., Amin, R., & Anderson, R. R. (2002). A new model of the location of the plasmapause: CRRES results. *Journal of Geophysical Research*, *107*(A11), 1339. https://doi.org/10.1029/2001JA009211

Nagano, H., Nishitani, N., & Hori, T. (2015). Occurrence characteristics and lowest speed limit of Sub-Auroral Polarization Stream (SAPS) observed by the SuperDARN Hokkaido East radar. *Earth, Planets and Space*, *67*(1), 126. https://doi.org/10.1186/s40623-015-0299-7

Nishida, A. (1966). Formation of plasmapause, or magnetospheric plasma knee, by the combined action of magnetospheric convection and plasma escape from the tail. *Journal of Geophysical Research*, *71*(23), 5669–5679. https://doi.org/10.1029/JZ071i023p05669

Nishida, A. (1968). Coherence of geomagnetic DP2 fluctuations with interplanetary magnetic variations. *Journal of Geophysical Research*, *73*(17), 5549–5559. https://doi.org/10.1029/JA073i017p05549

O'Brien, T. P., & Moldwin, M. B. (2003). Empirical plasmapause models from magnetic indices. *Geophysical Research Letters*, *30*(4), 1152. https://doi.org/10.1029/2002GL016007

Otsuka, Y., Ogawa, T., Saito, A., Tsugawa, T., Fukao, S., & Miyazaki, S. (2002). A new technique for mapping of total electron content using GPS network in Japan. *Earth, Planets and Space*, *54*(1), 63–70. https://doi.org/10.1186/BF03352422

Park, C. G. (1973). Whistler observations of the depletion of the plasmasphere during a magnetospheric substorm. *Journal of Geophysical Research*, *78*(4), 672–683. https://doi.org/10.1029/JA078i004p00672

Picone, J. M., Hedin, A. E., Drob, D. P., & Aikin, A. C. (2002). NRLMSISE-00 empirical model of the atmosphere: Statistical comparisons and scientific issues. *Journal of Geophysical Research*, *107*(A12), 1468. https://doi.org/10.1029/2002JA009430

Redmon, R. J., Seaton, D. B., Steenburgh, R., He, J., & Rodriguez, J. V. (2018). September 2017's geoeffective space weather and impacts to Caribbean radio communications during hurricane response. *Space Weather*, *16*, 1190–1201. https://doi.org/10.1029/2018SW001897

Richards, P. G., Fennelly, J. A., & Torr, D. G. (1994). EUVAC: A solar EUV flux model for aeronomic calculations. *Journal of Geophysical Research*, *99*(A5), 8981–8992. https://doi.org/10.1029/94JA00518

Richards, P. G., Meier, R. R., & Wilkinson, P. J. (2010). On the consistency of satellite measurements of thermospheric composition and solar EUV irradiance with Australian ionosonde electron density data. *Journal of Geophysical Research*, *115*, A10309. https://doi.org/10.1029/2010JA015368

Richards, P. G., Thomas, N., Woods, T. N., & Peterson, W. K. (2006). HEUVAC: A new high resolution solar EUV proxy model. *Advances in Space Research*, *37*(2), 315–322. https://doi.org/10.1016/j.asr.2005.06.031

Richmond, A. D. (1995). Ionospheric electrodynamics using magnetic apex coordinates. *Journal of Geomagnetism and Geoelectricity*, *47*(2), 191–212. https://doi.org/10.5636/jgg.47.191

Richmond, A. D., & Maute, A. (2014). Ionospheric electrodynamics modeling. In J. D. Huba et al. (Eds.), *Modeling the Ionosphere-Thermosphere*, *Geophysical Monograph Series* (Vol. 201, Chap. 6). Washington, DC: American Geophysical Union.

Rodger, A. (2008). The mid-latitude trough—Revisited. In P. M. Kintner, Jr., A. J. Coster, T. J. Fuller-Rowell, A. J. Mannucci, M. Mendillo, & R. Heelis (Eds.), *Midlatitude ionospheric dynamics and disturbances*, *geophysical monograph series*, (Vol. 181, pp. 25–33). Washington, DC: American Geophysical Union.

Sandel, B. R., King, R. A., Forrester, W. T., Gallagher, D. L., Broadfoot, A. L., & Curtis, C. C. (2001). Initial results from the IMAGE extreme ultraviolet imager. *Geophysical Research Letters*, *28*(8), 1439–1442. https://doi.org/10.1029/2001GL012885

Scherliess, L., & Fejer, B. G. (1999). Radar and satellite global equatorial *F* region vertical drift model. *Journal of Geophysical Research*, *104*(A4), 6829–6842. https://doi.org/10.1029/1999JA900025

Shinbori, A., Otsuka, Y., Tsugawa, T., Nishioka, M., Kumamoto, A., Tsuchiya, F., et al. (2018). Temporal and spatial variations of storm time midlatitude ionospheric trough based on global GNSS-TEC and Arase satellite observations. *Geophysical Research Letters*, *45*, 7362–7370. https://doi.org/10.1029/2018GL078723

Shprits, Y. Y., Li, W., & Thorne, R. M. (2006). Controlling effect of the pitch angle scattering rates near the edge of the loss cone on electron lifetimes. *Journal of Geophysical Research*, *111*, A12206. https://doi.org/10.1029/2006JA011758

Sibeck, D. G., Takahashi, K., Yumoto, K., & Reeves, G. D. (1998). Concerning the origin of signatures in dayside equatorial ground magnetograms. *Journal of Geophysical Research*, *103*(A4), 6763–6769. https://doi.org/10.1029/97JA03600

Spasojević, M., Goldstein, J., Carpenter, D. L., Inan, U. S., Sandel, B. R., Moldwin, M. B., & Reinisch, B. W. (2003). Global response of the plasmasphere to a geomagnetic disturbance. *Journal of Geophysical Research*, *108*(A9), 1340. https://doi.org/10.1029/2003JA009987

Summers, D., & Thorne, R. M. (2003). Relativistic electron pitch angle scattering by electromagnetic ion cyclotron waves during geomagnetic storms. *Journal of Geophysical Research*, *108*(A4), 1143. https://doi.org/10.1029/2002JA009489

Sun, Y.-Y., Matsuo, T., Maruyama, N., & Liu, J.-Y. (2015). Field-aligned neutral wind bias correction scheme for global ionospheric modeling at midlatitudes by assimilating FORMOSAT-3/COSMIC h_mF_2 data under geomagnetically quiet conditions. *Journal of Geophysical Research: Space Physics*, *120*, 3130–3149. https://doi.org/10.1002/2014JA020768

Thomsen, M. F. (2004). Why *Kp* is such a good measure of magnetospheric convection. *Space Weather*, *2*, S11004. https://doi.org/10.1029/2004SW000089

Tsugawa, T., Kotake, N., Otsuka, Y., & Saito, A. (2007). Medium-scale traveling ionospheric disturbances observed by GPS receiver network in Japan: A short review. *GPS Solutions*, *11*(2), 39–144. https://doi.org/10.1007/s10291-006-0045-5

Tsugawa, T., Nishioka, M., Ishii, M., Hozumi, K., Saito, S., Shinbori, A., et al. (2018). Total electron content observations by dense regional and worldwide international networks of GNSS. *Journal of Disaster Research*, *13*(3), 535–545.

Tsuji, Y., Shinbori, A., Kikuchi, T., & Nagatsuma, T. (2012). Magnetic latitude and local time distributions of ionospheric currents during a geomagnetic storm. *Journal of Geophysical Research*, *117*, A07318. https://doi.org/10.1029/2012JA017566

Tsurutani, B., Mannucci, A., Iijima, B., Abdu, M. A., Sobral, J. H. A., Gonzalez, W., et al. (2004). Global dayside ionospheric uplift and enhancement associated with interplanetary electric fields. *Journal of Geophysical Research*, *109*, A08302. https://doi.org/10.1029/2003JA010884

Walsh, B. M., Foster, J. C., Erickson, P. J., & Sibeck, D. G. (2014). Simultaneous ground- and space-based observations of the plasmaspheric plume and reconnection. *Science*, *343*(6175), 1122–1125. https://doi.org/10.1126/science.1247212

Wei, Y., Fraenz, M., Dubinin, E., He, M., Ren, Z., Zhao, B., et al. (2013). Can a nightside geomagnetic Delta H observed at the equator manifest a penetration electric field? *Journal of Geophysical Research: Space Physics*, *118*, 3557–3567. https://doi.org/10.1002/jgra.50174

Weimer, D. R. (1996). A flexible, IMF dependent model of high-latitude electric potentials having “space weather” applications. *Geophysical Research Letters*, *23*(18), 2549–2552. https://doi.org/10.1029/96GL02255

Yizengaw, E., & Moldwin, M. B. (2005). The altitude extension of the midlatitude trough and its correlation with plasmapause position. *Geophysical Research Letters*, *32*, L09105. https://doi.org/10.1029/2005GL022854

Yumoto, K., & the MAGDAS Group (2006). MAGDAS project and its application for space weather. In N. Gopalswamy, & A. Bhattacharyya (Eds.), *Solar Influence on the Heliosphere and Earth's Environment: Recent Progress and Prospects*, (pp. 309–405). Quest Publications for ILWS and Indian Institute of Geomagnetism. https://cdaw.gsfc.nasa.gov/publications/ilws_goa2006